Eurographics/ ACM SIGGRAPH Symposium on Computer Animation (2016)
Ladislav Kavan and Chris Wojtan (Editors)

Two-way Coupling of Fluids to Reduced Deformable Bodies

Wenlong Lu[1†] Ning Jin[1†] Ronald Fedkiw[12†]

[1]Stanford University [2]Industrial Light + Magic

Abstract

We propose a fully monolithic two-way coupling framework that couples incompressible fluids to reduced deformable bodies. Notably, the resulting linear system matrix is both symmetric and positive-definite. Our method allows for the simulation of interesting free-surface as well as underwater phenomena, enabling the use of reduced deformable bodies as full-fledged simulation primitives alongside rigid bodies and deformable bodies. Momentum conservation is crucial to obtaining physically correct and realistic-looking motion in a fluid environment, and we achieve this by following previous work to describe reduced deformable bodies using both a rigid frame and a reduced space deformation component. Our approach partitions forces and impulses between the reduced space and the rigid frame of the reduced deformable bodies using a projection scheme that cleanly accounts for momentum losses in the reduced space via corrections in the rigid frame, resulting in a new theoretical formulation for the momentum-conserving reduced deformable body. We demonstrate that robust and stable contact, collision, articulation, and two-way coupling with fluids are all attainable in a straightforward way using this new formulation. Compared with fully deformable objects, our framework consumes less memory and scales better in large scenes, while still nicely approximating the deformation effects.

Categories and Subject Descriptors (according to ACM CCS): I.3.7 [Computer Graphics]: Three-Dimensional Graphics and Realism—Animaion

1. Introduction

For solid/fluid coupling, one could employ fully deformable bodies, see for example [GSLF05,CGFO06,RMSG*08], but quite often the modes are highly damped, especially by liquids, and therefore the deformable objects do not typically exhibit much non-rigid motion. Thus, many authors instead use rigid body approximations, see e.g. [CMT04, GSLF05, KFCO06, BBB07, RMSG*08]. However, the rigid approximation, while simple and fast, sometimes appears overly dull since it does not allow for any deformations. In this sense, reduced deformable bodies seem to be good intermediaries between rigid bodies and fully deformable bodies. Moreover, many deformable underwater creatures such as jellyfish generate motions with non-local actuation modes making reduced models particularly well suited for simulating these features. In addition, if a simulation contains many copies of the same creature, for instance the starfish in Figure 10, then rigid bodies only need one copy of the triangulated surface and implicit surface shared amongst all objects (see [GBF03]), whereas deformable bodies would require full copies of all relevant data structures for every object. In this scenario, reduced deformable bodies also scale like rigid bodies, benefiting from the cheap representation where only the rigid mode and the small reduced mode vector need to be stored independently for each individual object.

Solid/fluid coupling algorithms focus on the balance of momentum between the solid and the fluid, and often prefer symmetry in regards to their associated linear systems so that solvers converge efficiently. Thus, we utilize the recent momentum preserving work of [SLYF15] which leverages the rigid frame proposed in [TW88]. See also [MT92, WMW15]. Unfortunately, the method in [SLYF15], while momentum conserving, does not provide a clean set of equations that can be used for solid/fluid coupling. Therefore, we begin by reconsidering their approach from the standpoint of projection matrices where one projects various forces onto the reduced space as well as the rigid frame and looks at potential losses in momentum as well as corrections to remedy these losses. This leads us directly to a novel retreatment of the approach in [SLYF15] based on a theoretically sound projection formulation with equations that are readily foldable into a monolithic solid/fluid coupling framework, fully preserving the associated momentum. The resulting linear system matrix is symmetric and positive-definite.

Notably, while more theoretically formal, our treatment still allows for extensions for all the interesting features considered in [SLYF15]. For example, it is more straightforward to incorporate collision and contact algorithms as well as the required impulses

† e-mail: {wenlongl|njin19|rfedkiw}@stanford.edu

© 2016 The Author(s)
Eurographics Proceedings © 2016 The Eurographics Association.

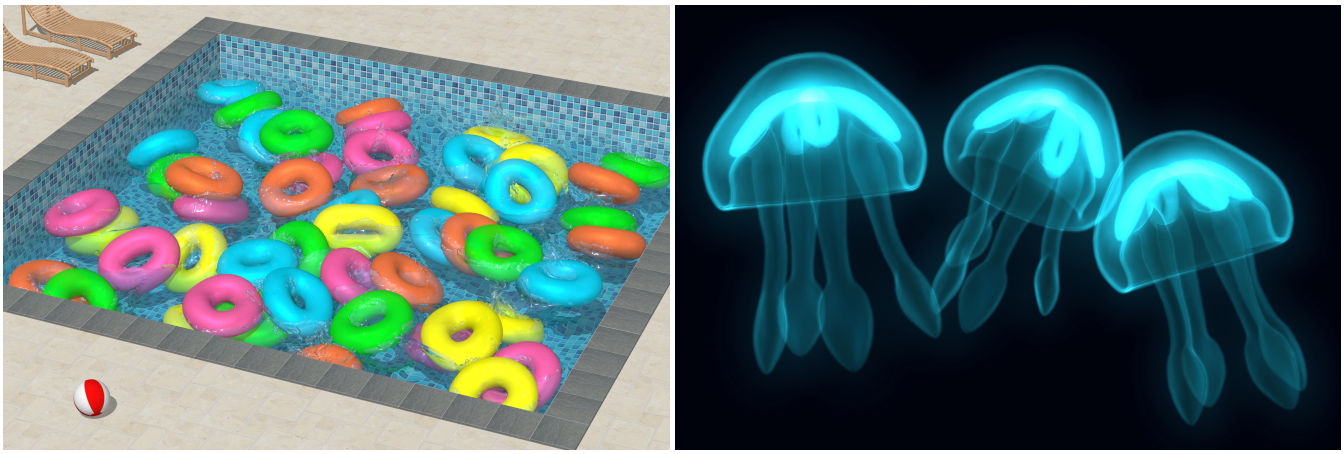

Figure 1: *Examples of reduced deformable bodies in our monolithic solid/fluid coupling framework. (Left) Fifty tori are dropped into a pool colliding with each other and making splashes. (Right) Three articulated and skinned jellyfish swim in deep water.*

using our projection formulation, e.g., see Figure 10. In addition, we also propose a fully implicitly coupled treatment for articulation between sub-components of reduced deformable bodies. In particular, our new framework incorporates the ability to skin the articulated sub-bodies as well. See Figures 8 and 9.

2. Related Work

Besides the works mentioned throughout the paper, we comment on a few other related works here. [PW89] introduced the modal analysis framework to approximate non-rigid behaviors with a subset of vibrational modes. To more accurately simulate larger deformations, [CK05] extended modal analysis to track local rotations and warp the modal basis. Nonlinear model reduction approaches such as the modal derivative method proposed in [IC85] have also been widely employed. For example, [BJ05] precomputed the coefficients of high order polynomials to achieve real-time simulations for the St. Venant-Kirchhoff materials. In addition to Euclidean space methods, an alternative rotation-strain subspace formulation was presented in [HTZ*11], and was adopted in [SvTSH14] for simulating deformation in keyframe animation. [PBH15] further corrected kinetic energy for the rotation-strain subspace simulation. A different class of methods that are not based on reduced basis construction have also been studied, for example, shape matching in [MHTG05] and its fast lattice version in [RJ07].

Hybrid representations for deformable objects have been introduced in [TW88] where a reference component is used to track rigid motion and a displacement component is used for deformation. Similarly, [MT92] partitioned a deformable body into a rigid part, a global deformation part, and a local deformation part, with applications in constrained dynamics of multibody objects. This idea is further adopted in the momentum conserving reduced deformable body framework in [SLYF15]. We also refer the readers to [FLLP13], which presented a hybrid Eulerian-on-Lagrangian framework where the Lagrangian modes describe rigid motion and global deformation along with the Eulerian representation of the local high frequency deformation. The idea of embeding deformation within a rigid frame is also widely used in the finite element methods for multibody simulation, where it is often referenced as the floating frame of reference formulation [SS98, BCS01, Sha05]. Articulation and skinning for reduced deformable bodies have been addressed in [KJP02, Sha05, KJ11, SLYF15].

The solid/fluid coupling framework used in this paper is developed based on [RMSF11]. See also [GSLF05, CGFO06, RMSG*08] for reference. For readers who are interested in reduced fluid simulation (although this is not within the scope of this paper), please refer to [Oha04, TLP06, WST09, KD13, LMH*15, ATW15] for more details.

3. Reduced Deformable Body Model

Similar to [TW88] and [SLYF15], we embed our reduced deformable model into a rigid frame

$$\vec{x} = \mathbf{R}(S\vec{q} + \vec{x}_0) + \vec{\mathbf{T}}, \tag{1}$$

where $\mathbf{R}$ is a block diagonal matrix of rotations R, $\vec{\mathbf{T}}$ is a vector of translations $\vec{t}$, S consists of the reduced modes, $\vec{q}$ are the reduced displacements, $\vec{x}_0$ are the rest positions. The mass-weighted column sums of S are 0 so that $S\vec{q} + \vec{x}_0$ contains no center of mass translation. Differentiating Equation 1 gives us

$$\vec{v} = \mathbf{R}S\dot{\vec{q}} + \dot{\mathbf{R}}(S\vec{q} + \vec{x}_0) + \dot{\vec{\mathbf{T}}}, \tag{2}$$

where the last two terms represent the angular and linear velocity of the rigid frame. The velocity of the rigid frame can be written as $v_{\text{rigid}} = \left(v_{\text{com}}, \omega_R\right)^T$, where v_{com} is the velocity of the center of mass, and ω_R is the angular velocity defined via $\dot{R} = \omega_R^* R$, where $*$ represents the skew-symmetric cross product matrix for a given vector. Defining $\vec{\mathbf{r}} = \mathbf{R}(S\vec{q} + \vec{x}_0)$ as column vector of moment arms allows us to rewrite Equation 2 as

$$\vec{v} = \mathbf{R}S\dot{\vec{q}} + \omega_R^*\vec{\mathbf{r}} + \dot{\vec{\mathbf{T}}} = \mathbf{R}S\dot{\vec{q}} + J_{\text{rigid}}v_{\text{rigid}}, \tag{3}$$

where J_{rigid} is an n by 2 block matrix where the first column consists of identity matrices $\delta_{3\times 3}$ and the second column consists of 3

© 2016 The Author(s)
Eurographics Proceedings © 2016 The Eurographics Association.

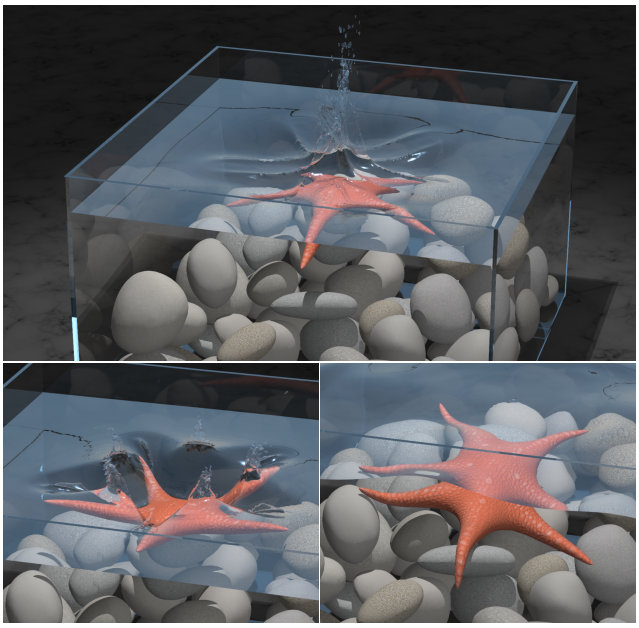

Figure 2: *A reduced deformable starfish (20 modes) deforms as it falls into the water and rests on the rocks (192×192×192 fluid grid).*

by 3 matrices of the form $\vec{r}_i^{*T}$:

$$J_{\text{rigid}} = \begin{pmatrix} \delta_{3\times 3} & \vec{r}_1^{*T} \\ \delta_{3\times 3} & \vec{r}_2^{*T} \\ \vdots & \vdots \\ \delta_{3\times 3} & \vec{r}_n^{*T} \end{pmatrix}. \tag{4}$$

Differentiating Equation 3 gives us

$$\ddot{\vec{x}} = \mathbf{R}S\ddot{\vec{q}} + \vec{F}^{\text{fict}}, \tag{5}$$

where $\vec{F}^{\text{fict}}$ are the so-called fictitious forces, which should be treated as acceleration. Using Newton's second law

$$M\mathbf{R}^{-1}\ddot{\vec{x}} = \vec{F}^{\text{int}} + \mathbf{R}^{-1}\vec{F}^{\text{ext}}, \tag{6}$$

where M is either a consistent or a diagonal mass matrix, we obtain

$$M_r\ddot{\vec{q}} = S^T\vec{F}^{\text{int}} + S^T\mathbf{R}^{-1}\vec{F}^{\text{ext}} - S^TM\mathbf{R}^{-1}\vec{F}^{\text{fict}}, \tag{7}$$

where $M_r = S^TMS$ is the reduced mass matrix. We define a combined external and fictitious forces as $\vec{F}^{\text{ef}} = \vec{F}^{\text{ext}} - \mathbf{R}M\mathbf{R}^{-1}\vec{F}^{\text{fict}}$, and rewrite Equation 7 as

$$M_r\ddot{\vec{q}} = S^T\vec{F}^{\text{int}} + S^T\mathbf{R}^{-1}\vec{F}^{\text{ef}}. \tag{8}$$

A simple linearized finite element model is used for the internal forces,

$$\vec{F}_r^{\text{int}} = S^T\vec{F}^{\text{int}} = -S^TKS\vec{q} - S^TCS\dot{\vec{q}} = -K_r\vec{q} - C_r\dot{\vec{q}}, \tag{9}$$

with Rayleigh damping, i.e., $C = \alpha M + \beta K$. Note that in all our examples we set $\alpha = 0$.

4. External Impulses

For the rigid frame, we define the diagonal matrix $M_{\text{rigid}} = J_{\text{rigid}}^TMJ_{\text{rigid}}$ whose upper left and lower right components are the rigid body mass and inertia tensor. If M is a diagonal mass matrix, one can verify that this gives the standard rigid mass m and inertia tensor I for a set of rigidified particles. When M is a consistent mass matrix, one obtains the standard rigid body mass, and we take the resulting inertia tensor as our definition of the rigid body inertia tensor for a consistent mass matrix. Given a set of impulses $\vec{\lambda}$ on the particles, the change in velocity of the particles is given by

$$\Delta\vec{v} = J_{\text{rigid}}M_{\text{rigid}}^{-1}J_{\text{rigid}}^T\vec{\lambda}. \tag{10}$$

This expresses the change in velocity of every particle on the rigid body given impulses simultaneously applied to every particle on the rigid body. Notably, if only one particle has $\lambda_i \neq 0$, and we only care about the change in velocity Δv_i of that particle, then Equation 10 reduces to the usual $\Delta v_i = (m^{-1}\delta_{3\times 3} + \vec{r}_i^{*T}I^{-1}\vec{r}_i^{*})\lambda_i$. Equation 10 generalizes this to be from the impulses on all particles to the velocity changes of all particles. Next we define

$$P_{\text{rigid}} = MJ_{\text{rigid}}M_{\text{rigid}}^{-1}J_{\text{rigid}}^T, \tag{11}$$

noting that P_{rigid} is a true projection where $P_{\text{rigid}}^2 = P_{\text{rigid}}$ can be trivially shown using the definition of M_{rigid}. A similar force projection is also explored in [MGL*15]. Thus, given any set of impulses $\vec{\lambda}$ on the particles, $P_{\text{rigid}}\vec{\lambda}$ gives a new set of impulses on the particles which conserves the momentum from $\vec{\lambda}$, and $(\delta_{n\times n} - P_{\text{rigid}})\vec{\lambda}$ represents the remaining portion of the impulses that do not affect the underlying motion of the rigid frame. Hence Equation 10 can also be expressed as

$$\Delta\vec{v} = M^{-1}P_{\text{rigid}}\vec{\lambda}. \tag{12}$$

Similar to P_{rigid}, P_{rigid}^T defines a projection that filters the rigid component out of the changes in particle velocities, i.e.,

$$\Delta\vec{v} = P_{\text{rigid}}^TM^{-1}\vec{\lambda}, \tag{13}$$

which is an equivalent form of Equations 10 and 12. In fact, we may also equivalently write

$$\Delta\vec{v} = P_{\text{rigid}}^TM^{-1}P_{\text{rigid}}\vec{\lambda}, \tag{14}$$

where P_{rigid} filters the impulses and P_{rigid}^T filters the velocities.

For the reduced space, $\vec{F}^{\text{ext}}$ in Equation 7 illustrates how impulses affect the reduced degrees of freedom, i.e., they are first multiplied by $S^T\mathbf{R}^{-1}$ before being multiplied by M_r^{-1} to obtain the changes in reduced velocities $\Delta\vec{q}$. Multiplying $\Delta\vec{q}$ by $\mathbf{R}S$ gives the equivalent change in velocity of the particles, i.e.,

$$\Delta\vec{v} = \mathbf{R}SM_r^{-1}S^T\mathbf{R}^{-1}\vec{\lambda}. \tag{15}$$

Similar to Equation 11, we define

$$P_r = M\mathbf{R}SM_r^{-1}S^T\mathbf{R}^{-1}, \tag{16}$$

where $P_r^2 = M\mathbf{R}SM_r^{-1}S^T\mathbf{R}^{-1}M\mathbf{R}SM_r^{-1}S^T\mathbf{R}^{-1}$, and the term in the middle $S^T\mathbf{R}^{-1}M\mathbf{R}S$ can be viewed as an M-weighted inner product that is not affected by the rotation of S by $\mathbf{R}$. Therefore

© 2016 The Author(s)
Eurographics Proceedings © 2016 The Eurographics Association.

Figure 3: *Comparison of a rigid starfish (left) and a reduced deformable starfish with 20 modes (right). The reduced deformable starfish exhibits compelling motion whereas its rigid counterpart appears stiff and boring.*

$S^T\mathbf{R}^{-1}M\mathbf{R}S = S^TMS = M_r$ proving $P_r^2 = P_r$. Similar to Equation 14, we may rewrite Equation 15 as

$$\Delta\vec{v} = P_r^T M^{-1} P_r \vec{\lambda}. \tag{17}$$

In the case of fully deformable objects with $S = \delta_{n\times n}$, we designate $P_d\vec{\lambda} = (\delta_{n\times n} - P_{\text{rigid}})\vec{\lambda}$ as the deformable component of the impulses, where $P_d^2 = P_d$. Thus, we could decompose any vector of impulses $\vec{\lambda}$ into $P_{\text{rigid}}\vec{\lambda}$ and $P_d\vec{\lambda}$, applying $P_{\text{rigid}}\vec{\lambda}$ to the rigid frame and $P_d\vec{\lambda}$ to the non-rigid deformable degrees of freedom. This gives the same result as applying the full $\vec{\lambda}$ to all the particles, and subsequently subtracting out the rigid frame. Unfortunately, due to P_r and P_{rigid} not being orthogonal, $P_r\vec{\lambda}$ and $P_{\text{rigid}}\vec{\lambda}$ do not partition the impulses in the same way that $P_d\vec{\lambda}$ and $P_{\text{rigid}}\vec{\lambda}$ do.

To have a momentum conserving partition scheme for the reduced deformable objects, we begin by mimicking the ideal setting applying $P_{\text{rigid}}\vec{\lambda}$ to the rigid frame and $P_d\vec{\lambda}$ to the reduced space. However, the reduced deformable body being lossy only applies $P_rP_d\vec{\lambda}$ as illustrated in Equation 17, leaving $(\delta_{n\times n} - P_r)P_d\vec{\lambda}$ unapplied not conserving momentum. Thus, we need to apply $(\delta_{n\times n} - P_r)P_d\vec{\lambda}$ to the rigid frame as a momentum correction. This turns out to be identical to the method proposed in [SLYF15]. Hence the net impulse applied to the rigid frame should be $(P_{\text{rigid}} + (\delta_{n\times n} - P_r)P_d)\vec{\lambda} = (\delta_{n\times n} - P_rP_d)\vec{\lambda}$. Note that as the number of modes of the reduced deformable model increases, the correction $(\delta_{n\times n} - P_r)P_d\vec{\lambda}$ goes to 0 and we smoothly approach the fully deformable case.

Consider the net change in velocity obtained by applying $P_rP_d\vec{\lambda}$ via Equation 17 and the correction $(\delta_{n\times n} - P_r)P_d\vec{\lambda}$ via Equation 14, i.e.,

$$\Delta\vec{v} = P_r^T M^{-1} P_r P_r P_d \vec{\lambda} + P_{\text{rigid}}^T M^{-1} P_{\text{rigid}} (\delta_{n\times n} - P_r) P_d \vec{\lambda}, \tag{18}$$

which can be rewritten as

$$\Delta\vec{v} = (\delta_{n\times n} - P_{\text{rigid}}^T) M^{-1} P_r P_d \vec{\lambda} = P_d^T M^{-1} P_r P_d \vec{\lambda}, \tag{19}$$

where we have used $P_r^2 = P_r$, $P_{\text{rigid}}P_d = 0$, $P_r^T M^{-1} P_r = M^{-1}P_r$, and $P_{\text{rigid}}^T M^{-1} P_{\text{rigid}} = P_{\text{rigid}}^T M^{-1}$. Again using $M^{-1}P_r = P_r^T M^{-1} P_r$ finally gives

$$\Delta\vec{v} = P_d^T P_r^T M^{-1} P_r P_d \vec{\lambda}. \tag{20}$$

Notably, if only one particle has $\lambda_i \neq 0$ and we only care about the change in velocity of that particle, then Equation 20 reduces to the impulse factor (K_2) in [SLYF15]. Moreover, one can see that the optional external forces projection in their paper (our P_d) is not optional at all, and omission of this would lead to asymmetry in their impulses, i.e., one cannot maintain symmetry by applying $P_r\vec{\lambda}$ via Equation 17 and $(\delta_{n\times n} - P_r)\vec{\lambda}$ via Equation 14.

Note that Equation 20 can be rewritten as

$$\Delta\vec{v} = P_d^T \mathbf{R} S M_r^{-1} S^T \mathbf{R}^{-1} P_d \vec{\lambda} \tag{21}$$

using Equation 16. We will refer back to this later at the end of Section 5.3.

5. Solid/Fluid Coupling

5.1. Fluid Equations

We use a standard MAC grid to discretize the incompressible fluid, and split the Navier-Stokes equations into two steps. First, we compute an intermediate fluid velocity ignoring pressure

$$\vec{u}^{\,*} = \vec{u}^{\,n} - \Delta t(\vec{u}^{\,n}\cdot\nabla)\vec{u}^{\,n} + \frac{\Delta t}{\rho}\vec{f}. \tag{22}$$

Then we solve the Poisson equation

$$\nabla\cdot\left(\frac{\Delta t}{\rho}\nabla p\right) = \nabla\cdot\vec{u}^{\,*}, \tag{23}$$

and apply the resulting pressure to impose incompressibility

$$\vec{u}^{\,n+1} = \vec{u}^{\,*} - \frac{\Delta t}{\rho}\nabla p. \tag{24}$$

We use the particle level set method of [EMF02] for our liquid simulations.

5.2. Solid Equations

First, we apply the same projection to the combined external and fictitious forces that we applied for impulses in Section 4, giving $P_rP_d\Delta t\vec{F}^{\text{ef}}$ to the reduced space and $(\delta_{n\times n} - P_rP_d)\Delta t\vec{F}^{\text{ef}}$ to the rigid frame:

$$M_r\dot{\vec{q}}^{\,\text{ef}} = M_r\dot{\vec{q}}^{\,n} + S^T\mathbf{R}^{-1}P_rP_d\Delta t\vec{F}^{\text{ef}}, \tag{25}$$

$$M_{\text{rigid}}v_{\text{rigid}}^{\text{ef}} = M_{\text{rigid}}v_{\text{rigid}}^{n} + J_{\text{rigid}}^T(\delta_{n\times n} - P_rP_d)\Delta t\vec{F}^{\text{ef}}. \tag{26}$$

Then, we apply the same treatment to internal forces $\mathbf{R}\vec{F}^{\text{int}}$ to obtain

$$M_r\dot{\vec{q}}^{\,n+1} = M_r\dot{\vec{q}}^{\,\text{ef}} + S^T\mathbf{R}^{-1}P_rP_d\Delta t\mathbf{R}\vec{F}^{\text{int}}, \tag{27}$$

$$M_{\text{rigid}}v_{\text{rigid}}^{n+1} = M_{\text{rigid}}v_{\text{rigid}}^{\text{ef}} + J_{\text{rigid}}^T(\delta_{n\times n} - P_rP_d)\Delta t\mathbf{R}\vec{F}^{\text{int}}. \tag{28}$$

Equations 27 and 28 reduce to

$$M_r\dot{\vec{q}}^{\,n+1} = M_r\dot{\vec{q}}^{\,\text{ef}} - \Delta tK_r\vec{q}^{\,n+1} - \Delta tC_r\dot{\vec{q}}^{\,n+1}, \tag{29}$$

$$M_{\text{rigid}}v_{\text{rigid}}^{n+1} = M_{\text{rigid}}v_{\text{rigid}}^{\text{ef}} - J_{\text{rigid}}^T M\mathbf{R}SM_r^{-1}\Delta t\vec{F}_r^{\text{int}}. \tag{30}$$

© 2016 The Author(s)
Eurographics Proceedings © 2016 The Eurographics Association.

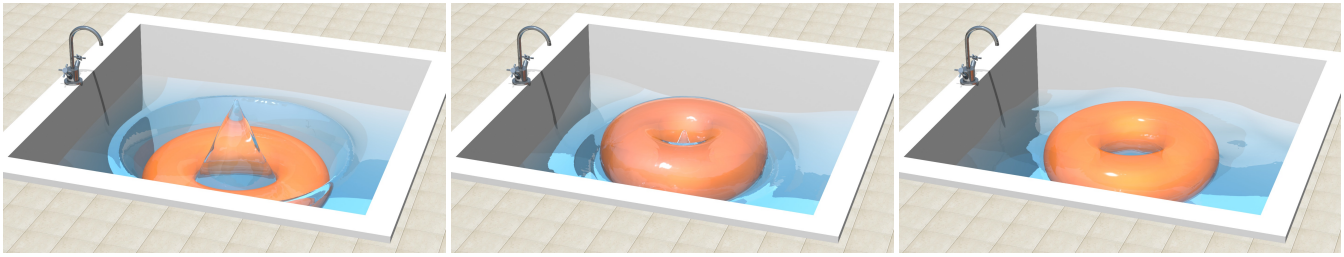

Figure 4: *A reduced deformable torus (10 modes) is dropped into a tub (192×192×192 fluid grid). The torus deforms as it goes into the water, and eventually reaches an equilibrium floating in the tub.*

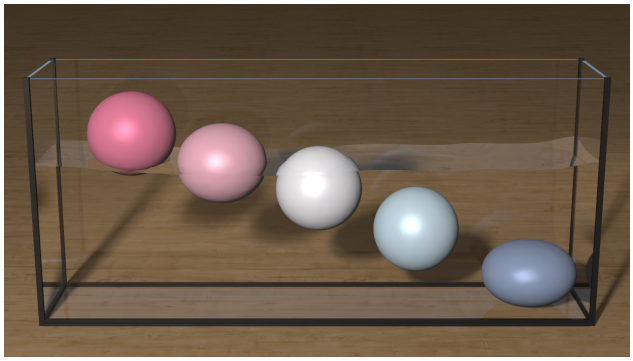

Figure 5: *Five reduced deformable spheres (each with 10 modes) with increasing densities from left to right are released in a water tank (320×64×176 fluid grid) and achieve equilibrium at different depths, illustrating that our method treats buoyancy properly.*

Figure 6: *15 reduced deformable tori (each with 10 modes) are dropped into a pool (384×384×128 fluid grid). The top figure illustrates the dynamics when the tori just hit the water riding on waves and making splashes. The bottom left figure shows the tori falling into the pool, and the bottom right figure shows them settling down.*

Using $\vec{q}^{\,n+1} = \vec{q}^{\,n} + \Delta t \dot{\vec{q}}^{\,n+1}$ allows us to rewrite Equation 29 as

$$(M_r + \Delta t C_r + (\Delta t)^2 K_r)\dot{\vec{q}}^{\,n+1} = M_r \dot{\vec{q}}^{\,\mathrm{ef}} - \Delta t K_r \vec{q}^{\,n}. \tag{31}$$

Next, we introduce intermediate explicitly computed velocities $\dot{\vec{q}}^{\,*}$ and v^*_{rigid} via

$$M_r \dot{\vec{q}}^{\,*} = M_r \dot{\vec{q}}^{\,\mathrm{ef}} - \Delta t K_r \vec{q}^{\,n}, \tag{32}$$

$$M_{\mathrm{rigid}} v^*_{\mathrm{rigid}} = M_{\mathrm{rigid}} v^{\mathrm{ef}}_{\mathrm{rigid}} + J^T_{\mathrm{rigid}} M \mathbf{R} S M_r^{-1} \Delta t K_r \vec{q}^{\,n}. \tag{33}$$

Finally, letting $\hat{M}_r = M_r + \Delta t C_r + (\Delta t)^2 K_r$ and $D_r = C_r + \Delta t K_r$, we have

$$\hat{M}_r \dot{\vec{q}}^{\,n+1} = M_r \dot{\vec{q}}^{\,*}, \tag{34}$$

$$M_{\mathrm{rigid}} v^{n+1}_{\mathrm{rigid}} = M_{\mathrm{rigid}} v^*_{\mathrm{rigid}} + J^T_{\mathrm{rigid}} M \mathbf{R} S M_r^{-1} \Delta t D_r \dot{\vec{q}}^{\,n+1}. \tag{35}$$

Note that these are the same equations that appear in [SLYF15], except that we cleanly separate forces utilizing $P_r P_d$ and $\delta_{n\times n} - P_r P_d$. This same clean separation could also be utilized by [WMW15].

5.3. Coupling

Letting $\beta = \rho V$ be the dual cell mass (where dual cells are cells between two adjacent pressure freedoms on the primal axis), and $\vec{\lambda}$ designate the impulses from solids to fluids, we modify Equations 24 to obtain

$$\beta \vec{u}^{\,n+1} = \beta \vec{u}^{\,*} - \hat{G}\hat{p} + W^T \vec{\lambda}. \tag{36}$$

where $\hat{G}$ and $-\hat{G}^T$ are the volume weighted gradient and divergence operators, and W is the matrix of 0's and 1's that selects the solid/fluid constraint faces. See [RMSF11]. Combining it with the divergence free equation,

$$-\hat{G}^T \vec{u}^{\,n+1} = 0, \tag{37}$$

gives us the modified discretized version of Equation 23:

$$\hat{G}^T \beta^{-1} \hat{G}\hat{p} - \hat{G}^T \beta^{-1} W^T \vec{\lambda} = G^T \vec{u}^{\,*}. \tag{38}$$

Letting J be the matrix that interpolates from solid particles to all non-solid dual cell centers, we augment Equations 34 and

© 2016 The Author(s)
Eurographics Proceedings © 2016 The Eurographics Association.

35 with an equal and opposite impulse $-J^T W^T \vec{\lambda}$, distributing $-P_r P_d J^T W^T \vec{\lambda}$ to Equation 34 and $-(\delta_{n\times n} - P_r P_d) J^T W^T \vec{\lambda}$ to Equation 35 to obtain

$$\hat{M}_r \dot{\vec{q}}^{\,n+1} = M_r \dot{\vec{q}}^{\,*} - S^T \mathbf{R}^{-1} P_r P_d J^T W^T \vec{\lambda}, \tag{39}$$

$$M_{\text{rigid}} v_{\text{rigid}}^{n+1} = M_{\text{rigid}} v_{\text{rigid}}^{*} + J_{\text{rigid}}^T M \mathbf{R} S M_r^{-1} \Delta t D_r \dot{\vec{q}}^{\,n+1} - J_{\text{rigid}}^T (\delta_{n\times n} - P_r P_d) J^T W^T \vec{\lambda}. \tag{40}$$

Using the typical equal velocity constraint to set the fluid velocity from Equation 36 equal to the solid velocity from Equation 3 interpolated to the dual cell center center via J results in

$$W(\vec{u}^{\,n+1} - J(\mathbf{R} S \dot{\vec{q}}^{\,n+1} + J_{\text{rigid}} v_{\text{rigid}}^{n+1})) = 0. \tag{41}$$

Substituting $\vec{u}^{\,n+1}$, $\dot{\vec{q}}^{\,n+1}$, and v_{rigid}^{n+1} from Equations 36, 39, and 40 results in

$$-W\beta^{-1}\hat{G}\hat{p} + W\beta^{-1}W^T\vec{\lambda} + WJK_\lambda J^T W^T \vec{\lambda} = rhs, \tag{42}$$

where the symmetric impulse factor K_λ is

$$K_\lambda = P_{\text{rigid}}^T M^{-1} P_{\text{rigid}} + P_d^T \mathbf{R} S \hat{M}_r^{-1} S^T \mathbf{R}^{-1} P_d, \tag{43}$$

and the rhs is

$$-W(\vec{u}^{\,*} - J\vec{v}^{\,*}) + WJP_d^T \mathbf{R} S(\hat{M}_r^{-1} M_r - \delta_{r\times r})\dot{\vec{q}}^{\,*}, \tag{44}$$

with $\vec{v}^{\,*} = \mathbf{R} S \dot{\vec{q}}^{\,*} + J_{\text{rigid}} v_{\text{rigid}}^{*}$. Equations 38 and 42 yield a symmetric positive-definite monolithic solid/fluid coupling system

$$\begin{pmatrix} \hat{G}^T\beta^{-1}\hat{G} & -\hat{G}^T\beta^{-1}W^T \\ -W\beta^{-1}\hat{G} & W\beta^{-1}W^T + WJK_\lambda J^T W^T \end{pmatrix} \begin{pmatrix} \hat{p} \\ \vec{\lambda} \end{pmatrix} = \begin{pmatrix} G^T \vec{u}^{\,*} \\ rhs \end{pmatrix}, \tag{45}$$

where the coefficient matrix is identical to that obtained in [RMSF11] with their inverse mass matrix replaced by K_λ. In fact, setting $S = 0$ results in $K_\lambda = J_{\text{rigid}} M_{\text{rigid}}^{-1} J_{\text{rigid}}^T$ making Equation 45 identical to the one proposed in [RMSF11] for the rigid body case (as long as one first interpolates to the particles).

Finally, note that the last term in Equation 43 has the same form as Equation 21, except that the presence of $\hat{M}_r^{-1}$ (which includes C_r and K_r) in Equation 43 does not allow us to recover a form similar to Equation 20.

6. Time Integration

We adopt the Newmark integration scheme from [QYF15] for the solid/fluid coupled evolution. In order to update the positions, we start with $\vec{u}^{\,n}$ and $\vec{v}^{\,n}$ and apply explicit forces for half a time step $\Delta t/2$ to obtain $\hat{u}^{\,*}$ and $\hat{v}^{\,*}$. Subsequently, we solve our coupled system to obtain $\vec{u}^{\,n+1/2}$ and $\vec{v}^{\,n+1/2}$. Next, we update the solid positions to time t^{n+1}. Collision and contact are resolved for the solid bodies using $\vec{x}^{\,n+1}$ and $\vec{v}^{\,n}$ to obtain a collision-free velocity $\tilde{v}^n$, which is accomplished by applying the momentum conserving impulses given in [SLYF15] (see also our Section 4). Finally, to update the velocities, we start with $\vec{u}^{\,n}$ and $\tilde{v}^{\,n}$ and take a full time step Δt. Explicit forces are used to evolve $\tilde{v}^{\,n}$ to $\vec{v}^{\,*}$, and $\vec{u}^{\,n}$ is updated to include explicit forces and advection to obtain $\vec{u}^{\,*}$. Then, we again solve our coupled system to obtain the t^{n+1} velocities $\vec{v}^{\,n+1}$ and $\vec{u}^{\,n+1}$.

7. Articulation and Skinning

Simulating more geometrically complex objects such as the jellyfish in Figures 8 and 9 is challenging using simple linear modes due to linearized rotation artifacts. [SLYF15] proposed simulating smaller components of such objects using linear modes, and subsequently articulating thse smaller components together. It is problematic to articulate objects under water by applying impulses in a post-process, since the water will tend to drive the objects toward one another. Although this is alleviated by the impulses in the post-process, the water velocities being unaware of the post-process will tend to discontinuously flow into the solid objects causing the water to lose volume. Thus we instead show how to incorporate articulation style impulses into our monolithic solid/fluid coupling solve.

Suppose we are articulating an arbitrary point x_p on body p to an arbitrary point x_c on body c. Let J_{ap} and J_{ac} be sparse matrices that interpolate from all particles to x_p and x_c respectively. We enforce articulation by applying an equal and opposite impulse $\vec{\lambda}_a$ to both bodies via $J_{ap}^T \vec{\lambda}_a$ and $-J_{ac}^T \vec{\lambda}_a$. This is accomplished by replacing $-J^T W^T \vec{\lambda}$ in Equations 39 and 40 with $-J^T W^T \vec{\lambda} + (J_{ap}^T - J_{ac}^T)\vec{\lambda}_a$. This gives a modified version of Equation 42

$$-W\beta^{-1}\hat{G}\hat{p} + W\beta^{-1}W^T\vec{\lambda} + WJK_\lambda J^T W^T \vec{\lambda} - WJK_\lambda (J_{ap}^T - J_{ac}^T)\vec{\lambda}_a = rhs, \tag{46}$$

where the rhs stays unchanged. Enforcing the equal velocity constraint gives $J_{ap}\vec{v}^{\,n+1} = J_{ac}\vec{v}^{\,n+1}$ where $\vec{v}^{\,n+1} = \mathbf{R} S \dot{\vec{q}}^{\,n+1} + J_{\text{rigid}} v_{\text{rigid}}^{n+1}$ as per Equation 3. Substituting the aforementioned equations into this equation yields

$$(J_{ac} - J_{ap}) K_\lambda J^T W^T \vec{\lambda} + (J_{ap} K_\lambda J_{ap}^T + J_{ac} K_\lambda J_{ac}^T)\vec{\lambda}_a = rhs_a, \tag{47}$$

where rhs_a is

$$(J_{ac} - J_{ap})(\vec{v}^{\,*} + P_d^T \mathbf{R} S(\hat{M}_r^{-1} M_r - \delta_{r\times r})\dot{\vec{q}}^{\,*}). \tag{48}$$

This becomes a new third equation in our system

$$\begin{pmatrix} A_{2\times 2} & 0 \\ 0 & a_{23} \\ 0 & a_{23}^T & a_{33} \end{pmatrix} \begin{pmatrix} \hat{p} \\ \vec{\lambda} \\ \vec{\lambda}_a \end{pmatrix} = \begin{pmatrix} G^T \vec{u}^{\,*} \\ rhs \\ rhs_a \end{pmatrix}, \tag{49}$$

where $A_{2\times 2}$ is our previously defined coupling matrix in Equation 45, $a_{23} = WJK_\lambda(J_{ac}^T - J_{ap}^T)$, and $a_{33} = J_{ap}K_\lambda J_{ap}^T + J_{ac}K_\lambda J_{ac}^T$. Notably, the system matrix remains symmetric and positive-definite. It is worth mentioning that this approach also works in order to fully monolithically couple articulation to the implicit formulation for reduced deformable bodies even without water. In that case, Equation 49 reduces to $a_{33}\vec{\lambda}_a = rhs_a$ where we solve for $\vec{\lambda}_a$ and subsequently substitute into the appropriate forms of Equations 39 and 40 to obtain $\dot{\vec{q}}$ and v_{rigid}.

To correct for position drift from numerical errors, we further apply pre-stabilization impulses following the approach in [WTF06]. This is done outside of our coupled system during the position update.

Although simulated separately, the articulated bodies are rendered using a standard skinning approach. This has implications on the simulation as described in [SLYF15], wherein the weights on particles used to create the skin mesh play a role in collision, contact,

© 2016 The Author(s)
Eurographics Proceedings © 2016 The Eurographics Association.

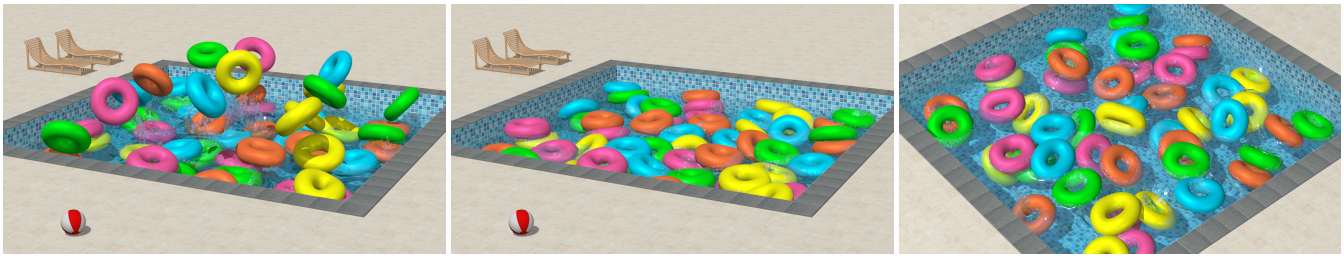

Figure 7: *50 reduced deformable tori (each with 10 modes) fall into a pool (256×256×64 fluid grid) and float on water (viewed from two different camera angles). The reduced deformable tori get squeezed and bent as they interact with the fluid and collide with each other.*

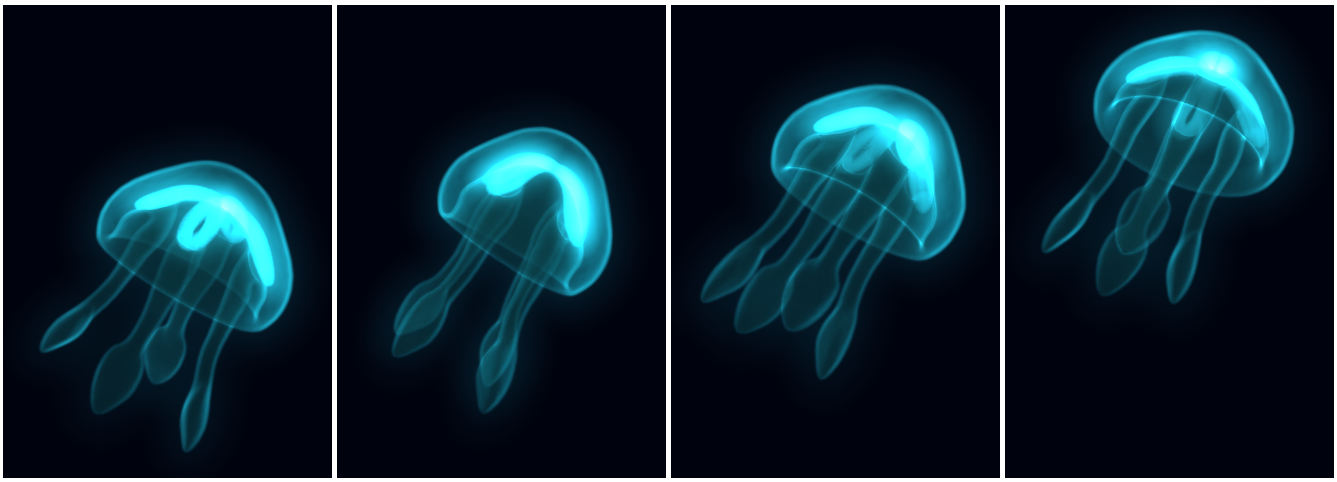

Figure 8: *An articulated and skinned reduced deformable jellyfish (5 sub-components each with 20 modes) swims in deep water (128×128×160 fluid grid). Balanced actuation forces are applied to eight points on the bottom of the bell to simulate the swimming motion.*

etc. We similarly incorporate skin particles by changing the matrix J (see Section 5.3) to include the effects of first weighting the solid particles to create the skin particles and then interpolating from the skin particles to all non-solid dual cell centers. J still effectively interpolates from the solid particles to the non-solid dual cell centers as in Section 5.3, but the weights change to incorporate the fact that the fluid should see the velocity of the skin mesh.

Figure 9: *Three articulated and skinned jellyfish swim closely together (128×128×160 fluid grid). Actuation forces are applied in the same manner as in the single jellyfish example in Figure 8. We assign different initial velocities to each jellyfish. The two jellyfish on the left bump into each other before heading off in different directions.*

© 2016 The Author(s)
Eurographics Proceedings © 2016 The Eurographics Association.

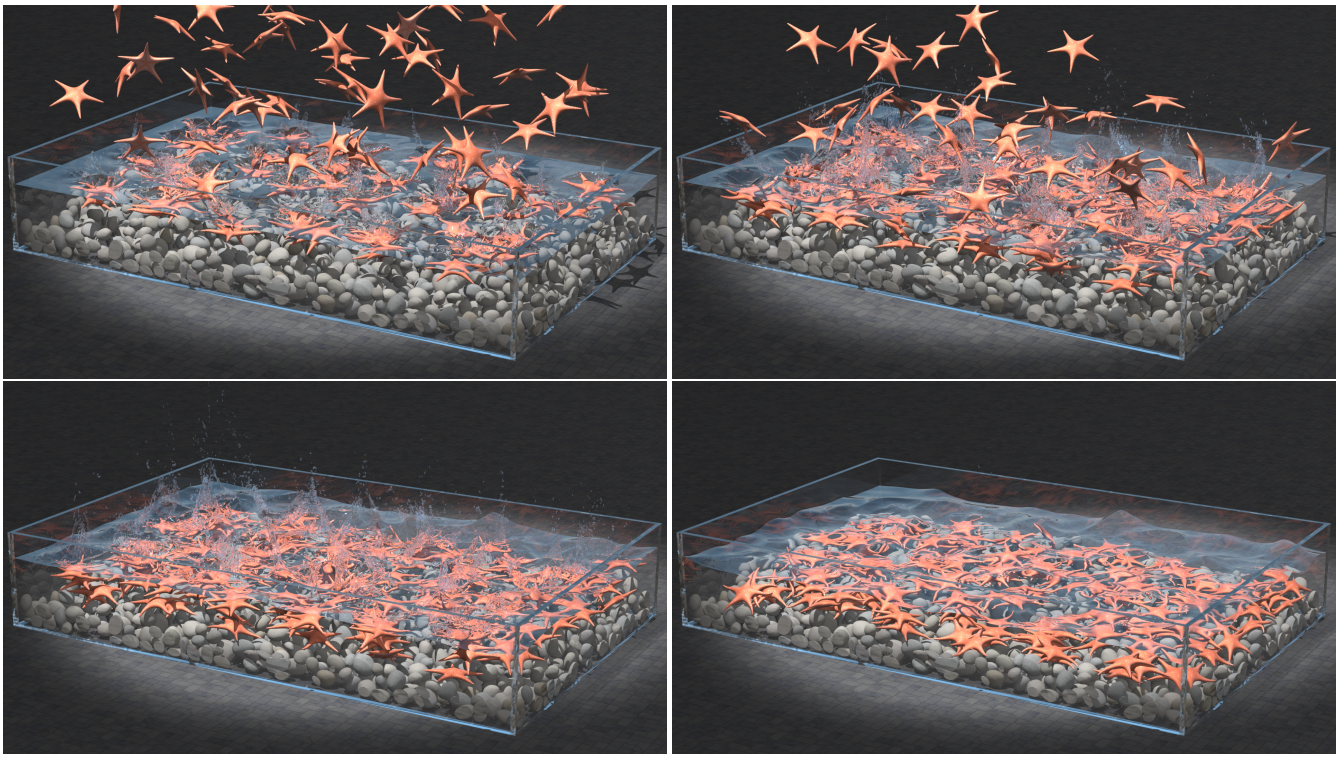

Figure 10: *150 reduced deformable starfish (each with 20 modes) fall into the water (224×352×64 fluid grid) and eventually settle down onto the rocks. The starfish are actuated by applying balanced forces to the five arms and the center of mass. These forces scale as a sine function in time. This example demonstrates the scalability of our framework and the ability to incorporate collision and contact correctly.*

8. Examples

In Figure 5, we provide a simple test to show that our method handles buoyancy properly. The density of the five reduced deformable spheres increases monotonically from left to right. The spheres are released from the same depth in the water tank and eventually settle at different depths ranging from floating to neutral to sinking. The sphere model has 2k vertices and 9k tetrahedrons. The water tank is $5m \times 1m$ with water filled up to 1.5 meters.

We use three different torus simulations to showcase applications of our coupling system. The torus model has 12k vertices and 60k tetrahedrons. Firstly, in Figure 4, we zoom in on a single torus to observe its deformation as well as the rich water features. When the torus first enters the water, it sinks down a little and the tube radius shrinks. After riding up and down several tides of waves, the torus eventually recovers its shape and floats on the water. The water in the tub is initially $1m \times 1m$ and filled up to 0.4 meters. Secondly, Figure 6 shows 15 tori dropped into a pool of size $3m \times 3m$ with warer filled up to 0.4 meters. Thirdly, in Figure 7 we make a even larger scale scene with 50 tori dropped into a bigger pool of size $4m \times 4m$ and water level again at 0.4 meters. These examples illustrate our capacity to properly incorporate collisions for a large number of floating objects.

Apart from simple shapes such as spheres and tori, we also ran our system on interesting sea creatures such as starfish and jellyfish. Figure 3 compares the motion of a rigid starfish and a reduced deformable starfish as they fall into a water tank. The starfish model has 2k vertices and 6k tetrahedrons. With only 20 reduced modes, the reduced deformable starfish is able to display quite compelling deformation as it hits water and then gently rests on the rocks, while the rigid starfish shows rather uninteresting motion throughout the simulation (as seen in the video). The area of the water tank is $1m \times 1m$, with water initially filled up to 0.4 meters. In Figure 10, we drop 150 of the reduced deformable starfish into a larger tank of water ($3.5m \times 5.5m \times 0.5m$). The starfish exhibit realistic motion as they successively fall into the water from various random initial orientations, colliding with each other and the rocks. The heavy stacking in the final rest poses illustrates the robustness of our system in handling collisions and contact. Furthermore, this example underlines the advantage of our method when there exist many copies of the same reduced deformable object as they can share most of the data structures leading to efficiency in storage.

Figures 8 and 9 highlight our ability to incorporate articulation and skinning into our monolithic coupling framework. We segment the jellyfish model into 5 sub-components: the bell and the four arms. One set of the whole jellyfish has 11k vertices and 37k tetrahedrons. We enforce three point joint constraints between each arm and the bell (twelve in total). The balanced actuation forces act on eight points near the bottom of the bell and produce smooth swimming motion. In Figure 9, three jellyfish start with different

© 2016 The Author(s)
Eurographics Proceedings © 2016 The Eurographics Association.

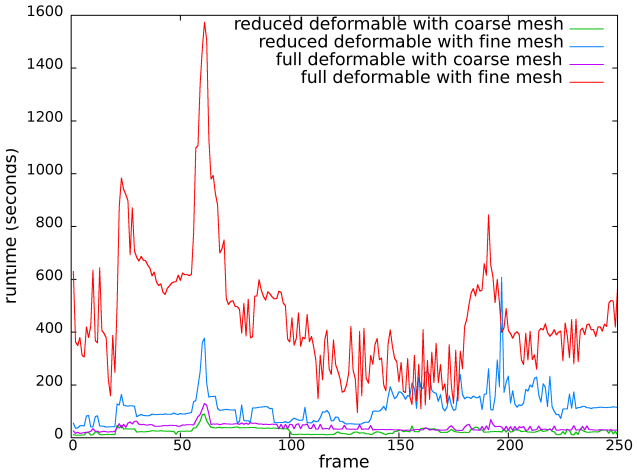

Figure 11: *The graph shows the runtime taken by each frame for the 50 tori performance tests. The first wave of tori hit the water surface around frame 20, and the second wave of tori hit the water surface around frame 60. Collision is turned off to make the simulations behave similar to each other.*

orientations and initial velocities. Note that we also passively advect some plankton nearby the jellyfish for the sake of added realism in visualization (see the video). Both simulation domains are $1m \times 1m \times 1.25m$.

In all the above-mentioned examples, we adopt the reduced deformable model described in Section 3, where the basis is computed following the modal analysis method [PW89], and thus the matrices M_r, D_r and $\hat{M}_r$ have a diagonal form. Notably, this makes the computation of $\hat{M}_r^{-1}$ in Equation 43 trivial.

To evaluate the performance of our coupling system compared to one that couples fluids to regular deformable bodies [RMSF11], we analyze the runtime needed by each system for the same problem. To make a fair comparison, we set up an example similar to that in Figure 7, where we spread out 50 tori evenly and drop them into the water without collision. We simulate this example with both a coarse torus mesh ($5k$ tetrahedra) and a fine torus mesh ($60k$ tetrahedra) using the two systems. The runtime per frame of the four simulations are shown in Figure 11. Note that more than 90% of the runtime is spent on the coupling system solve using the preconditioned conjugate gradient (PCG) method, which is the most expensive part in these examples, as well as all the other examples shown in this paper. While our system for reduced deformable body shows only marginal performance benefits over the system for regular deformable body on a coarse mesh, the advantages are more pronouced on higher resolution meshes. Although one could still argue that a regular deformable body with a coarse mesh can provide deformations with similar levels of detail to those of as a reduced body with a fine mesh, a regular deformable body could suffer from various problems that a reduced deformable body trivially avoids, including high frequency oscillation, and undesirable local deformations.

9. Conclusion

First, we formalized the projection scheme introduced in [SLYF15] to neatly partition forces and impulses between the reduced space and the rigid frame of the reduced deformable bodies in a manner that guarantees conservation of momentum. Then, we used this new framework in order to formulate a monolithic solid/fluid coupling approach that enables reduced deformable bodies to be simulated in a fluid environment along with their rigid and fully deformable counterparts. In addition, we illustrated how to fully couple articulated bodies into the solid/fluid coupling framework, and further included details for skinned bodies.

While reduced deformable bodies alone bring considerable savings in terms of computational resources and simulation time in comparison to fully deformable bodies, the benefits are less obvious in a solid/fluid coupling framework. For example, in Figure 6, where 15 tori were dropped into the water, the simulation still takes one minute per frame (depending on the degree to which the tori are interacting) because the overall simulation speed is bounded from below by the non-reduced fluid simulation. Nevertheless, our approach significantly reduces the storage for deformable bodies to be more along the lines of rigid bodies. Moreover, our method scales well to large number of objects with the same model, since each object only has a small constant number of degrees of freedom and they can share a majority of the data structures. Notably, this also substantially reduces the communication cost during parallelization. In addition, the smaller degrees of freedom could make it feasible to solve optimization problems for deformable bodies; for example, one could explore extensions of [TGTL11] to deformable swimming creatures. Finally, our framework provides a theoretical foundation that could be used to couple reduced deformable solids to model reduced fluids such as those mentioned in related work.

Acknowledgements

Research supported in part by ONR N00014-13-1-0346, ONR N00014-11-1-0707, ONR N-00014-11-1-0027, and ARL AHPCRC W911NF-07-0027. W. L. was supported in part by The VMware Fellowship Fund in honor of Ole Agesen. Computing resources were provided in part by ONR N00014-05-1-0479.

References

[ATW15] ANDO R., THÜREY N., WOJTAN C.: A dimension-reduced pressure solver for liquid simulations. In *Computer Graphics Forum* (2015), vol. 34, Wiley Online Library, pp. 473–480. 2

[BBB07] BATTY C., BERTAILS F., BRIDSON R.: A fast variational framework for accurate solid-fluid coupling. *ACM Trans. Graph. (SIGGRAPH Proc.) 26*, 3 (2007), 100. 1

[BCS01] BERZERI M., CAMPANELLI M., SHABANA A. A.: Definition of the elastic forces in the finite-element absolute nodal coordinate formulation and the floating frame of reference formulation. *Multibody System Dynamics 5*, 1 (2001), 21–54. 2

[BJ05] BARBIČ J., JAMES D.: Real-time subspace integration of St. Venant-Kirchhoff deformable models. *ACM Trans. Graph. (SIGGRAPH Proc.) 24*, 3 (2005), 982–990. 2

[CGFO06] CHENTANEZ N., GOKTEKIN T. G., FELDMAN B., O'BRIEN J.: Simultaneous coupling of fluids and deformable bodies. In *ACM SIGGRAPH/Eurographics Symp. on Comput. Anim.* (2006), pp. 325–333. 1, 2

© 2016 The Author(s)
Eurographics Proceedings © 2016 The Eurographics Association.

[CK05] CHOI M. G., KO H.-S.: Modal warping: Realtime simulation of large rotational deformation and manipulation. *IEEE Trans. on Vis. and Comput. Graph. 11* (2005), 91–101. 2

[CMT04] CARLSON M., MUCHA P. J., TURK G.: Rigid fluid: Animating the interplay between rigid bodies and fluid. *ACM Trans. Graph. (SIGGRAPH Proc.) 23* (2004), 377–384. 1

[EMF02] ENRIGHT D., MARSCHNER S., FEDKIW R.: Animation and rendering of complex water surfaces. *ACM Trans. Graph. (SIGGRAPH Proc.) 21*, 3 (2002), 736–744. 4

[FLLP13] FAN Y., LITVEN J., LEVIN D. I. W., PAI D. K.: Eulerian-on-lagrangian simulation. *ACM Trans. Graph. 32*, 3 (July 2013), 22:1–22:9. 2

[GBF03] GUENDELMAN E., BRIDSON R., FEDKIW R.: Nonconvex rigid bodies with stacking. *ACM Trans. Graph. 22*, 3 (2003), 871–878. 1

[GSLF05] GUENDELMAN E., SELLE A., LOSASSO F., FEDKIW R.: Coupling water and smoke to thin deformable and rigid shells. *ACM Trans. Graph. (SIGGRAPH Proc.) 24*, 3 (2005), 973–981. 1, 2

[HTZ*11] HUANG J., TONG Y., ZHOU K., BAO H., DESBRUN M.: Interactive shape interpolation through controllable dynamic deformation. *IEEE Trans. on Vis. and Comput. Graph. 17*, 7 (July 2011), 983–992. 2

[IC85] IDELSOHN S. R., CARDONA A.: A reduction method for nonlinear structural dynamic analysis. *Computer Methods in Applied Mechanics and Engineering 49*, 3 (1985), 253 – 279. 2

[KD13] KIM T., DELANEY J.: Subspace fluid re-simulation. *ACM Trans. Graph. 32*, 4 (July 2013), 62:1–62:9. 2

[KFCO06] KLINGNER B. M., FELDMAN B. E., CHENTANEZ N., O'BRIEN J. F.: Fluid animation with dynamic meshes. *ACM Trans. Graph. (SIGGRAPH Proc.) 25*, 3 (2006), 820–825. 1

[KJ11] KIM T., JAMES D. L.: Physics-based character skinning using multi-domain subspace deformations. In *Proceedings of the 2011 ACM SIGGRAPH/Eurographics Symposium on Computer Animation* (New York, NY, USA, 2011), SCA '11, ACM, pp. 63–72. 2

[KJP02] KRY P., JAMES D., PAI D.: Eigenskin: real time large deformation character skinning in hardware. In *Proc. of the ACM SIGGRAPH Symp. on Comput. Anim.* (2002), ACM Press, pp. 153–159. 2

[LMH*15] LIU B., MASON G., HODGSON J., TONG Y., DESBRUN M.: Model-reduced variational fluid simulation. *ACM Trans. Graph. 34*, 6 (Oct. 2015), 244:1–244:12. 2

[MGL*15] MALGAT R., GILLES B., LEVIN D. I. W., NESME M., FAURE F.: Multifarious hierarchies of mechanical models for artist assigned levels-of-detail. In *Proceedings of the 14th ACM SIGGRAPH / Eurographics Symposium on Computer Animation* (New York, NY, USA, 2015), SCA '15, ACM, pp. 27–36. 3

[MHTG05] MÜLLER M., HEIDELBERGER B., TESCHNER M., GROSS M.: Meshless deformations based on shape matching. *ACM Trans. Graph. (SIGGRAPH Proc.) 24*, 3 (2005), 471–478. 2

[MT92] METAXAS D., TERZOPOULOS D.: Dynamic deformation of solid primitives with constraints. In *Proc. of the 19th annual conf. on Comput. graph. and inter. tech.* (1992), SIGGRAPH '92, pp. 309–312. 1, 2

[Oha04] OHAYON R.: Reduced models for fluid–structure interaction problems. *International Journal for Numerical Methods in Engineering 60*, 1 (2004), 139–152. 2

[PBH15] PAN Z., BAO H., HUANG J.: Subspace dynamic simulation using rotation-strain coordinates. *ACM Trans. Graph. 34*, 6 (2015). 2

[PW89] PENTLAND A., WILLIAMS J.: Good vibrations: modal dynamics for graphics and animation. *Comput. Graph. (Proc. SIGGRAPH 89) 23*, 3 (1989), 215–222. 2, 9

[QYF15] QIU L., YU Y., FEDKIW R.: On thin gaps between rigid bodies two-way coupled to incompressible flow. *J. Comput. Phys. 292*, 0 (2015), 1 – 29. 6

[RJ07] RIVERS A., JAMES D.: FastLSM: Fast lattice shape matching for robust real-time deformation. *ACM Trans. Graph. 26*, 3 (2007). 2

[RMSF11] ROBINSON-MOSHER A., SCHROEDER C., FEDKIW R.: A symmetric positive definite formulation for monolithic fluid structure interaction. *J. Comput. Phys. 230*, 4 (2011), 1547–1566. 2, 5, 6, 9

[RMSG*08] ROBINSON-MOSHER A., SHINAR T., GRÉTARSSON J. T., SU J., FEDKIW R.: Two-way coupling of fluids to rigid and deformable solids and shells. *ACM Trans. Graph. (SIGGRAPH Proc.) 27*, 3 (Aug. 2008), 46:1–46:9. 1, 2

[Sha05] SHABANA A.: *Dynamics of Multibody Systems*. Cambridge University Press, 2005. 2

[SLYF15] SHETH R., LU W., YU Y., FEDKIW R.: Fully momentum-conserving reduced deformable bodies with collision, contact, articulation, and skinning. In *ACM SIGGRAPH/Eurographics Symp. on Comput. Anim.* (2015), pp. 45–54. 1, 2, 4, 5, 6, 9

[SS98] SHABANA A., SCHWERTASSEK R.: Equivalence of the floating frame of reference approach and finite element formulations. *International journal of non-linear mechanics 33*, 3 (1998), 417–432. 2

[SvTSH14] SCHULZ C., VON TYCOWICZ C., SEIDEL H.-P., HILDEBRANDT K.: Animating deformable objects using sparse spacetime constraints. *ACM Trans. Graph. 33*, 4 (2014), 109:1–109:10. 2

[TGTL11] TAN J., GU Y., TURK G., LIU C. K.: Articulated swimming creatures. In *ACM SIGGRAPH 2011 papers* (2011), SIGGRAPH '11, ACM, pp. 58:1–58:12. 9

[TLP06] TREUILLE A., LEWIS A., POPOVIĆ Z.: Model reduction for real-time fluids. *ACM Trans. Graph. 25*, 3 (2006), 826–834. 2

[TW88] TERZOPOULOS D., WITKIN A.: Physically based models with rigid and deformable components. In *Graph. Interface* (1988), pp. 146–154. 1, 2

[WMW15] WU X., MUKHERJEE R., WANG H.: A unified approach for subspace simulation of deformable bodies in multiple domains. *ACM Trans. Graph. 34*, 6 (2015), 241:1–241:9. 1, 5

[WST09] WICKE M., STANTON M., TREUILLE A.: Modular bases for fluid dynamics. *ACM Trans. Graph. 28*, 3 (2009), 1–8. 2

[WTF06] WEINSTEIN R., TERAN J., FEDKIW R.: Dynamic simulation of articulated rigid bodies with contact and collision. *IEEE TVCG 12*, 3 (2006), 365–374. 6

© 2016 The Author(s)
Eurographics Proceedings © 2016 The Eurographics Association.